High-performance imaging of cell-substrate contacts using refractive index quantification microscopy

ZIQIANG XIN,[1] CHONGLEI ZHANG,[1,4] LIXUN SUN,[1] CHAO WAN,[1] TING CHEN,[1] HOUKAI CHEN,[1] MIN WANG,[2] YIJIA WANG,[3] SIWEI ZHU,[3] AND XIAOCONG YUAN[1,5]

[1]*Nanophotonics Research Center, Shenzhen Key Laboratory of Micro-Scale Optical Information Technology & Institute of Microscale Optoelectronics, Shenzhen University, Shenzhen, 518060, China*
[2]*Photonics Center, Shenzhen University, Shenzhen, 518060, China*
[3]*Institute of Oncology, Tianjin Union Medical Center, Tianjin, 300121, China*
[4]*zhangsir071115@szu.edu.cn*
[5]*xcyuan@szu.edu.cn*

Abstract: Non-invasive imaging of living cells is an advanced technique that is widely used in the life sciences and medical research. We demonstrate a refractive index quantification microscopy (RIQM) that enables label-free studies of glioma cell-substrate contacts involving cell adhesion molecules and the extracellular matrix. This microscopy takes advantage of the smallest available spot created when an azimuthally polarized perfect optical vortex beam (POV) is tightly focused with a first-order spiral phase, which results in a relatively high imaging resolution among biosensors. A high refractive index (RI) resolution enables the RI distribution within neuronal cells to be monitored. The microscopy shows excellent capability for recognizing cellular structures and activities, demonstrating great potential in biological sensing and live-cell kinetic imaging.

1. Introduction

Cell adhesion (CA) and the extracellular matrix (ECM) are both important for cell growth, migration, communication, and regulation. Notably, the ECM plays a vital role in synaptic remodeling of active neurons, which is essential for memory formation [1]. Moreover, CA and the ECM could influence many physiological phenomena, such as the development and maintenance of tissues, wound healing, and tumor metastasis [2–5]. Events occurring at the cell-substrate interface affect CA and ECM behaviors significantly and the ability to observe the localization and real-time activity of these events plays an important role in biological studies [6]. The emergence of fluorescence labeling techniques has revolutionized the life sciences because of its super-resolution and highly endogenous contrast characteristics [7,8]. Due to the capacity of effective background noise suppression, total internal refection fluorescence microscopy (TIRFM) has emerged that provides clear fluorescence images within evanescent field and appears to be a promising tool for the study of cell-substrate contacts [9,10]. The subsequent variable-angle TIRFM (vaTIRFM) can reveal topography of cells by changing the incident angle of illuminating light [11,12]. However, fluorescence microscopy requires different fluorescent dyes to specifically identify proteins of interest within subcellular structures. It is sometimes undesirable to stain the cells of interest in certain applications (e.g. stem cell and fertility studies, neurotransmitter and conduction studies) [13], and the process of staining with multiple fluorophores can also be challenging.

Non-invasive biological microscopy is essential for a wide variety of biomedical studies. Compared with traditional fluorescent labeling, refractive index (RI) mapping enables subcellular

structures to be observed without the fluorescent labeling [14]. Owing to its label-free and non-invasive nature, RI imaging has great potential to complement fluorescence microscopic studies of specific cellular mechanisms [15,16]. Although phase contrast microscopy [17,18] and differential interference contrast microscopy [19,20] are most commonly used to enhance image contrast, the resulting contrast is only qualitative. Quantitative phase imaging techniques, including optical diffraction tomography, have developed rapidly to become a popular and powerful approach to cell imaging, with advantages including wide-field illumination and a high frame rate. However, the resulting RI images result from intensity differences across the entire optical path, which obscures details at cell-substrate interfaces. Moreover, the RI imaging sensitivity is limited by the light path error [13,21–27]. Among the developed methods of surface RI imaging, surface plasmonic resonance imaging (SPRi) is an outstanding analytical tool because of its superior RI sensitivity [28–33]. SPRi works within SPs, which are excited under a specific angle for microscopy, but the finite numerical aperture of objective lens may limit the potential applications if shorter light wave-lengths were needed [6]. Moreover, for the purpose of making cells adhere metal substrate in a good state, some measurements are necessary including adhesion protein deposited on metal surface [34], or even fabricating glass material covering the metal surface [35]. A similar RI microscopy method is based on the differential absorption of s- and p-polarized light by graphene [36–39], which requires the graphene substrate to be very flat without any defect. No matter SPRi or microscopy based on graphene, the fabrication of the substrates and operations on the substrate all complicate the imaging process.

Among label-free imaging techniques for cell-substrate contacts, there is one kind of technique which is based on Fresnel's theory [40–42] and utilizes glass substrate where cell cultures are more commonly grown than a metal film. Prism-based total internal reflection dark-field microscope (p-TIRDFM) [43], reflection interference contrast microscopy (RICM) [44,45] and total internal reflection holographic microscopy (TIRHM) [46–50] are all such techniques and capable of providing nanometer-scale information about the topography of membrane surface. In this paper, we present an RI quantification microscopy (RIQM) for imaging cell-substrate contacts which is similarly based on Fresnel's theory. Although RI images are obtained just by measuring the intensity of light reflected from a glass substrate, a relative high-level sensitivity of 10^{-6} RI unit (RIU) can be achieved comparing with the above-mentioned techniques. The change of the RI above the interface can be measured from the weak variations with lock-in amplification mechanism. Taking advantage of the ring-shaped and tunable diameter of a POV beam, the RIQM is fixed at a smallest spot size, which results in a relatively high imaging resolution among biosensors [51–55]. The POV beam is modulated to be azimuthally polarized with a first-order spiral phase, yielding the smallest possible spot size [38,39]. The single point sensor resolution reaches 496 nm, and the RI resolution is 9.709×10^{-6} RIU in experiment. In summary, RIQM of subcellular organelles and structures including CA regions and the ECM of neurons, can be achieved in the cell substratum, which is critically important in neurotechnology applications. Furthermore, RIQM of live-cell contraction can be performed in a fast-scanning method, demonstrating the method's excellent capability of recognizing cellular structures and dynamics.

2. Methods

2.1. Lithography

Glass cover slips (Thorlabs, CG15CH) were soaked in acetone solution to clear organic surface impurities, then Photoresist (AR-P679.03PMMA 950 K) was spread evenly over the surface using a spin coater. An electron beam lithography machine was used to the fabricate the grating sample. We designed three slits with different widths (100 nm, 150 nm, 200 nm), and these slits were marked with numbers 1, 2 and 3. The last step in the photoetching was to soak the lithography slip in the developing liquid and then in a fixing bath for 30 mins each.

Slit width calibration via atomic force microscopy was required. As illustrated in Supplementary Fig. S1, a width of 120 nm was determined.
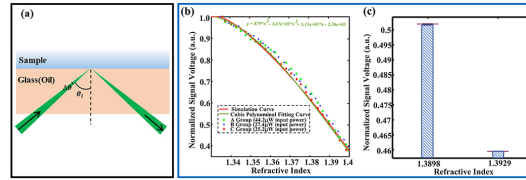
Fig. 1. The correlation between the detected signal and RI. (a) Schematic of interfacial reflection of light with average angle of incidence θ and width $\Delta\theta$. (b) Comparison of experimental data from three groups (points) and theoretical values using $\theta_i = 65.3°$ and $\Delta\theta_i = 8°$. A cubic polynomial fit of the data from group C is also shown (green line). (c) Boxplot of two data points from group C used for calculation of RI sensitivity.

2.2. Cell culture, fixation, and fluorescence labeling

The U-87 MG human neuroglioma cells were obtained from the American Type Culture Collection (ATCC) and maintained in Dulbecco's Modified Eagle's Medium (DMEM) (Gibco). The culture medium was supplemented with 10% fetal bovine serum (FBS) (Gibco), penicillin (100U, Gibco), and streptomycin (100U, Gibco). The cells were incubated at 37°C in a humidified incubator with 5% CO_2. The day before imaging, cells were seeded onto a cover slip to give 30-50% density.

For the fluorescence imaging assay, cells were transfected with CellLight Tubulin-RFP solution (Invitrogen). After incubation for 18-24 h, the culture medium was removed and the cells washed twice with phosphate buffered saline before 15 min fixation with 4% paraformaldehyde. After discarding the fixative, the cells were imaged using a Leica TCS SP8 microscope.

For the apoptosis assay, cells were either untreated or exposed to 8 μM paclitaxel solution for approximately 1 h.

2.3. Imaging principle and sensitivity

In Fresnel's theory, the intensity of light reflected from an interface is determined by the angle of incidence and the refractive indices of the two interfacial materials. Many studies have been devoted to the measurement of small changes in the RI of liquids and gases. Notably, McClimans et al. reported a prism-based real-time differential refractometry with a resolution-independent sensitivity of 10^{-6} RIU [41]. Total internal reflection fluorescence microscopy inspired Bohannon et al. to develop near-total internal reflection microscopy for the purpose of cellular RI imaging with a lateral resolution of 1 μm but inadequate sensitivity [42]. We have achieved both high RI sensitivity and imaging resolution using a tightly focused POV.

The reflectance of s-polarized light based on Fresnel's theory is given by:

$$R_s = -\frac{\sin(\theta_i - \theta_t)}{\sin(\theta_i + \theta_t)}. \tag{1}$$

where R_s is the reflection ratio of s-polarized light, and θ_i and θ_t are the angles of incidence and reflection, respectively, n represents the ratio of refractive indices n_2 and n_1 between optically denser and thinner media, respectively. Since the POV beam is modulated as azimuthal polarization, it will be s-polarized after tight focusing. When total internal reflection occurs, the

expression in Eq. (1) becomes:

$$R_s = \frac{\cos \theta_i - i\sqrt{\sin \theta_i^2 - n^2}}{\cos \theta_i + i\sqrt{\sin \theta_i^2 - n^2}}. \tag{2}$$

Combining the above equations, we obtain the relationship between the angle of incidence and the intensity of the reflected light. When carrying out experiments under the tight focusing condition, a small range of incident angles exists. Therefore, we allowed the angle of incidence to range from 61.3° to 69.3° in the numerical calculations (Fig. 1(b)), which agreed well with the experimental data.

To measure the RI sensitivity of the system, glycerol-water mixtures with different glycerol fractions were used to calibrate the relationship between detected signal voltages and the RIs measured using an Abbe refractometer. A microfluidic channel made from a polydimethylsiloxane (PDMS) was adhered to the surface of a cover slip, and used in combination with a syringe pump to inject the solutions. We carried out three groups of experimental measurements, as shown in Fig. 1(b). The laser input power used for group A was 44.2 μW, which was about twice that used for group B. Both experimental groups displayed a consistent relationship after normalization. In addition, the group C measurements were performed using a laser input power of 25.2 μW, and with a preamplifier placed before the digital data acquisition system (National Instruments) to improve the SNR. Cubic polynomial fitting of the normalized signal voltage measured for group C (Fig. 1(b), green curve) yielded the following relationship:

$$s = 879 \times n_x^3 - 3.67 \times 10^3 \times n_x^2 + 5.11 \times 10^3 \times n_x - 2.36 \times 10^3. \tag{3}$$

Consequently, Eq. (2) was used in all of cell imaging experiments to identify the cellular RI distributions. Figure. 1(c) shows the signal voltage data obtained using two solutions with different RIs (1.3898 and 1.3929). The RI sensitivity (RIS) is defined as:

$$RIS = \frac{\Delta n}{SNR}. \tag{4}$$

where $\Delta n = 0.0031$ represents the difference between the two RIs. The SNR between the two data groups can be determined using:

$$SNR = \frac{|\bar{s}_1 - \bar{s}_2|}{\sigma_1 + \sigma_2}. \tag{5}$$

where $\bar{s}_1 = 0.502(a.u.)$ and $\bar{s}_2 = 0.4595(a.u.)$ are the mean signal voltages for the two solutions, and $\sigma_1 = 6.888 \times 10^{-5}$, $\sigma_2 = 6.416 \times 10^{-5}$ are the corresponding standard deviations. Due to the usage of lock-in amplification, we acquired voltage signal steadily. As showed in Fig. 1(c), every box diagram contains one hundred continuous signals and the low standard deviation shows the stability. Here, by combining Eq. (3) and Eq. (4), the RIS is equal to 9.709×10^{-6} RIU and the systematic errors respectively are $\pm 5.056 \times 10^{-6}$ and $\pm 4.794 \times 10^{-6}$ by plugging the standard deviation and corresponding RI into Eq. (3). The approach described in this work is therefore a promising method for exploring low-RI subcellular structures, such as the ECM, with high sensitivity.

2.4. Setup of RIQM

A schematic of the RIQM instrument is depicted in Fig. 2(a). A semiconductor laser with high output power generates a 532 nm laser beam, which is incident onto a programmable spatial light modulator (SLM) (Holoeye, Pluto 3). An optical chopper (Thorlabs, MC200B-EC and

MC1F10HP) is placed before the SLM to change the continuous laser into a 10 MHz pulsed beam, which is then coordinated with the lock-in amplifier to improve the signal-to-noise ratio (SNR). The phase map on the SLM consists of the phase information of an axicon, a spiral phase, and a blazed grating. Therefore, a POV beam with explicit ring shape is generated and one of the diffraction orders is incident on photoelectric detector 1. Lenses 1 and 2 are used to collimate the beam, and the conjugate image of the POV ring is obtained at the rear focal plane of a high-numerical-aperture microscope objective (Olympus, 60×, NA = 1.42). Then a half-wave plate (Thorlabs, WPH05M-532) and a vortex plate (Thorlabs, WPV10L-532) are used to obtain a pure azimuthally polarized POV beam with a first-order spiral phase (Fig. 2(b)), which is tightly focused onto the sensor chip by the microscope objective (Fig. 1(c)). The principle of polarization modulation was demonstrated by Sun et al. [37]. Light reflected from the objective is collected using photoelectric detector 2 (Thorlabs, PDB210C), whose signal combines with the synchronizing signal from photoelectric detector 1 before entering the lock-in amplifier. In addition, a monitoring system based on bright-field imaging is included (Fig. 2(a)), "Illumination").
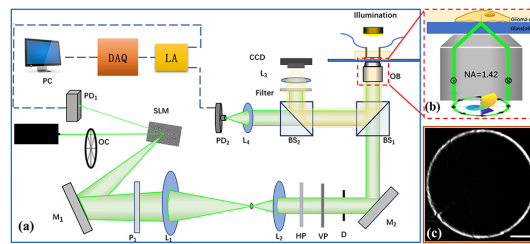

Fig. 2. (a) Schematic of the RI quantitative microscope. Abbreviations: OC: optical chopper; SLM: spatial light modulator; M1, M2: mirrors; L1, L2, L3, L4: lenses; P1: polarizer; HP: half-wave plate; VP: vortex plate; BS1, BS2: beam splitters; CCD: charge-coupled device; PD1, PD2: photoelectric detectors; LA: lock-in amplifier; DAQ: digital data acquisition system; PC: personal computer. (b) Schematic of the objective, the perfect optical vortex (POV) beam with finest ring width. Arrows indicate the POV is modulated as a pure azimuthal polarized beam and the central spiral map indicates a spiral phase from 0 to 2π. (c) Experimental POV beam at the rear focal plane of the objective with azimuthal polarization. Scale bar: 2 mm.

Currently, the RI maps are obtained by scanning with a two-dimensional electric translation stage and it is the number of data points that determines the imaging time. Every RI value at point acquired costs 30 ms during which the two-dimensional platform moves steadily in 400 nm step length. Thus, an RI map with 40 μm × 40 μm range may be obtained in 5 minutes.

2.5. Imaging resolution and penetration depth

To illustrate the advantages of polarization and phase modulation, we simulated the tightly focused spot of a POV beam with azimuthal polarization and first-order spiral phase [56–58]. Figures 3(a-c) show images of the intensity distributions of the x, y, and z components at the focal plane. These three components were added to obtain the total intensity distribution (Fig. 3(d)), from which a full width at half maximum value of 144 nm was obtained for the focused spot, which provides the ideal theoretical imaging resolution.

Before experimental measurement of spatial resolution, we used electron beam lithography (Raith, PIONEER Two) to fabricate a sample slit with a nominal width of 100 nm, whose bright-field image is shown in Fig. 3(f). The material used for the photoresist was polymethyl methacrylate (PMMA; AR-P 679.03), with an RI of 1.478 and a film thickness of 230 nm. Strict control of the exposure intensity is well known to be difficult, so it is essential to calibrate the slit
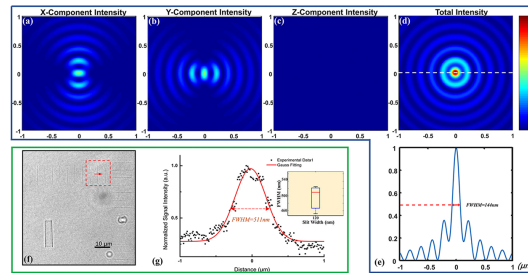
Fig. 3. Simulation of the tightly focused spot. Distribution of the (a) x, (b) y, and (c) z intensity components, and (d) the normalized total intensity at the focal plane. (e) Intensity profile along the white dashed line in panel d. (f) Lithographic slit structure on a bare glass plate. (g) One intensity profile data obtained by scanning across the slit shown in the red square in panel f. After applying a Gauss-function fitting, the FWHM indicates a 511 nm resolution. The inset plots the results from three experimental measurements,and the average resolution is 496nm.

width. We performed this task using an atomic force microscope (Bruker, Bioscope Catalyst), which yielded an average slit width of approximately 120 nm, below that of the focusing spot. During the experiments, a two-dimensional electric translation stage was used to scan across a single slit in 10 nm steps over a 5 μm range. One of experimentally measured groups is partly shown in Fig. 3(g). After a Gauss-function fitting, the full width half maximum (FWHM) of the focused spot, corresponding to the system resolution, was measured to be 511 nm, which is bigger than twice the general optical resolution ($0.61\lambda/NA = 228$ nm). The inset plots the results from three experimental measurements, and the average resolution is 496 nm. The other two experimental data groups are showed in Supplementary Fig. S2. Compared with the theoretical imaging resolution, the lower system resolution may be a consequence of interactions between multiple side lobes and the main lobe, as well as the evanescent field effect on the sample surface [59,60].

Theoretically, the cell region probed by RIQM is limited within evanescent field which is not exceeding a wavelength. Experimentally, we scanned a polystyrene (PS) bead to estimate the penetration depth of RIQM. A sketch of the interaction between the focal evanescent and PS bead is shown in Fig. 4(a). When moving away from the center of the bead, the sphere is no longer in contact with the glass surface. And the gap distance z increases as the geometrical relationship with the lateral position l: $z = r - \sqrt{r^2 - l^2}$, where r represents the radius of PS bead which is 1.5 μm. Notably, the contact point between bead and glass surface is hard to be determined in the experiment. We chose 8 data groups in an original two-dimension scanning map which's intensity is normalized and the maximum value of the chosen data is equal or greater than 0.99(a.u.). In Supplementary Fig. S3, the bright field image of the PS bead and an original map are demonstrated. The scanning range of the original map is 6 $\mu m \times 6$ μm and the scanning step length is 30 nm. By averaging these 8 data groups, the scatter diagram is demonstrated in Fig. 4(b). After polynomial fitting, we estimate the penetration depth of RIQM is about 384 nm in consideration of the attenuation coefficient "$1/e$".
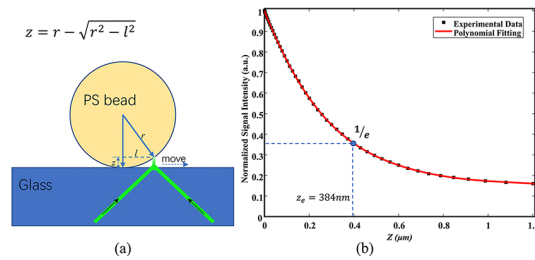
Fig. 4. Penetration depth of RIQM probed with a polystyrene bead, whose diameter is 3 μm. (a) Sketch of the focal field probed by the RIQM. (b) Normalized signal intensity varied with the gap distance z, and black dots are average experimental data from 8 groups.

3. Results and discussion

3.1. Comparison of RI imaging with conventional imaging

RI variations result directly from fluctuations in the density of cellular dry mass. The RI is therefore a powerful endogenous contrast agent [16]. Most of the cell dry mass is composed of proteins and phospholipids, with the former constituting a large proportion of the cytoplasm. CA plays an integral role in stimulating signals that regulate cell differentiation, cycle, migration, and survival. The affinity of cells for substrates is a crucial consideration in biomaterial design and development [3]. RI imaging of U-87 MG human neuroglioma cells was carried out in this study and mosaic RI images of two cells are presented in Fig. 5(a5) and Fig. 5(b4). Before the RI imaging experiment, the cells were fixed and imaged using a phase contrast microscope (Zeiss) and a fluorescence microscope (Leica) as shown in Figs. 5(a1-a4) and Figs. 5(b1-b3). Detailed cell processing methods are provided in the Methods part. Figure 5(a5) shows the RI images of two glioma cells connected via a synapse, which provides a clear view of subcellular structures, including the cell nucleus (high RI values are marked with red arrows). The consistency of the images obtained using each method demonstrates that the RI imaging technique reveals the true cellular morphology and that the point-scan imaging mechanism does not introduce aberrations. Notably, this label-free imaging technique requires no molecular staining and maintains cellular activity. Additionally, because the imaging depth of investigation is limited by the propagation range of the evanescent field, the RI image reflects the biological events that occur at the cell-substrate interface. For example, the region highlighted by the square in Fig. 5(b4) has different features compared with the phase contrast map in Fig. 5(b2). These bleb-like effects on the cell membrane are due to the paraformaldehyde cross-linking agents used for cell fixation. In addition, the circled and squared regions in Fig. 5(b4) exhibit more structural details than the phase contrast map in Fig. 5(b2). The fine line structure shown in the red squared region of Fig. 5(a5) demonstrates the high resolution that can be achieved using the proposed method; subcellular structures, such as organelles and bottom growing structures, are also clearly observed in the circled region.

3.2. Monitoring of cell contraction and ECM variation

Gliomas are the most common intracranial tumors and are associated with a median survival time of 15 months, even with aggressive therapy. This can be explained, in part, by the diffuse infiltration of single tumor cells into the brain parenchyma, which is thought to be a multi-factorial process involving interactions with the ECM [2,5]. Preventing invasion remains a key therapeutic goal and expansive efforts have been made to identify key molecular regulators of glioblastoma multiforme tumor cell motility in vitro [61]. Numerous studies have determined that the ECM is predominantly composed of fibronectin, collagen, fibrillin, and tenascin, all of
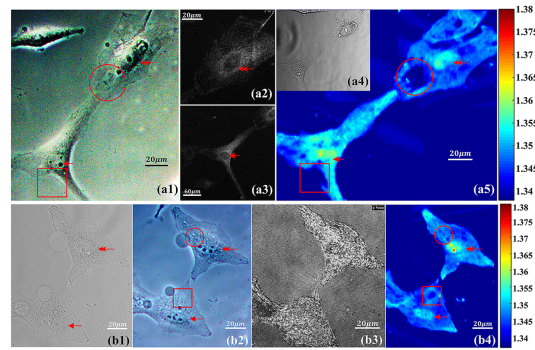
Fig. 5. (a1-a5) and (b1-b5) show two groups of U-87 MG human neuroglioma cells. Phase contrast maps (Zeiss) were obtained using a (a1) 20× and (b2) 40× objective. (a2,a3,b3) Corresponding fluorescence maps (Leica sp8) of tubulin labeled with red fluorescent protein. (a4,b1) Corresponding bright field images (Leica Sp8). (a5) RI mosaic of three images ($80\mu m \times 80\mu m$). (b4) RI mosaic of two images ($80\mu m \times 80\mu m$). Single- and double-headed arrows indicate the lower and upper cell nuclei, respectively. The circled and squared regions in panels a5 and b4 highlight some bleb-like structures that cannot be seen in the corresponding phase contrast images in panels a1 and b2, respectively. Additionally, the squared region in panel a1 shows a fine structure that also is clearly visible in panel a5, which demonstrates the high resolution that can be achieved.

which influence the migration of glioma cells [2]. However, the biophysical characteristics of ECM interactions remain poorly understood. It has been shown that the mechanical rigidity of the cellular micro-environment may alter the motility of glioma cells [61,62]. Here, we develop a simple imaging technique to obtain the RI distribution within cells, which is one of the most important biophysical parameters.

Cell growth, proliferation, and mutation can all lead to variation of RI distributions. Figure 6 demonstrates such monitoring of glioma cell (U-87 MG) contraction over a 4 h period, during which 37°C temperature and 5% CO_2 concentration were maintained. Figures 6(a0) and 6(b0) show bright-field images acquired at 0 h and 2.5 h, respectively. Figures 6(a1-a3) and (b1-b3) show the sequence of RI images obtained over a 4 h period. Before the imaging experiment, the RI of cell culture medium was determined to be 1.337 using an Abbe refractometer. The square region in Fig. 6 emphasizes the changes occurring at the synaptic junction during the contraction, while the red arrows indicate the positions of intracellular organelles, possibly being mitochondria. The ability to resolve organelles indicates the high-resolution advantage of the proposed method.

The combined results of the RI imaging demonstrate that the cell can be divided into four regions characterized by different RI values. Figure 7(a) shows the extracted image from Fig. 6(b1) that contains RI contours with values of 1.34, 1.343, 1.35, and 1.356. Compared with the fluorescence images reported in other studies [2,5], the contours in Fig. 7(a) divide the cell into four parts: region 1 clearly delineates the ECM; region 2 probably corresponds to the cytoplasm; region 3 is the area where most of the vinculins are located ; and region 4 corresponds to the position of the cell nucleus. To clarify the functions of these regions, we plotted the area ratio as a function of time (Fig. 7(b)). The area ratio of region 1 changes in the opposite manner to that of region 2, while regions 3 and 4 remain relatively stable and are almost equivalent. This illustrates that the cellular events mainly involve changes in the ECM, while the cytoplasm and regions near the nucleus remain relatively stable. Consequently, this RI imaging method provides clear insight into the changes occurring near the cell-substrate interface and is a
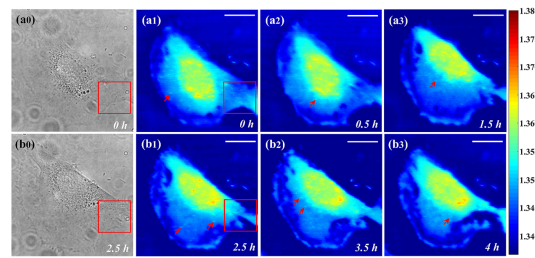
Fig. 6. Bright-field images are shown at (a0) 0 h and (b0) 2.5 h. (a1-a3,b1-b3) Monitoring of the RI evolution during cell contraction. Organelles are marked with arrows and a synaptic junction is located within the red square. The range of RI map is $80\mu m \times 80\mu m$. Scale bar: $20\mu m$.

promising tool for studying biophysical mechanisms occurring in living cells at the subcellular level, with potential applications in the life sciences and medical diagnosis.
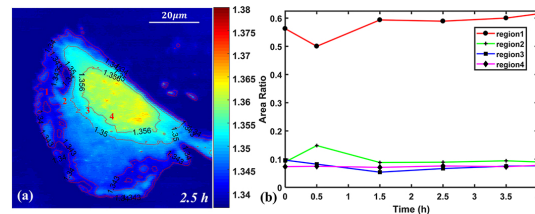

Fig. 7. RI image analysis. (a) The extracted image of Fig. 6(b1) with RI contour values of 1.34 (region 1), 1.343 (region 2), 1.35 (region 3), and 1.356 (region 4). (b) Time-dependent area ratios of regions 1-4.

3.3. Cell apoptosis assay

Paclitaxel has shown great potential as a cancer treatment. The cytotoxicity of paclitaxel is believed to be related to its ability to stabilize and enhance assembly of microtubules [63,64]. U-87 cells were cultured with or without 8 μM paclitaxel solution for more than 1 h, during which time the RI distributions of individual glioma cells were measured (Fig. 8). The RI images of an untreated cell in Figs. 8(a1-d1) reveal the gradual decomposition of the structures within the red square, as reflected by the decrease in the RI in this region. Additionally, red arrows identify a prominent subcellular organelle in the RI images, which provide greater detail compared with the bright-field images shown in Figs. 8(a0-d0). During paclitaxel treatment cell (Figs. 8(e1-h1)), some constantly changing high-RI regions were identified (red arrows) and the apoptosis appeared to induce cellular clumping and detachment in a shorter time (c.f. Figs. 8(a1-d1)). These differences can be attributed to the stabilization of microtubules by paclitaxel.

3.4. Monitoring of a synapse

Among the many types of cells, neurons are highly polarized and have distinct subcellular compartments, including one or more dendritic processes emerging from the cell body, and a single, extended axon that is involved in intercellular communications with them [65]. These connections take place in synapses generated between axons of presynaptic neurons and dendrites of postsynaptic neurons, and are central to the study of neuroscience. We used RIQM to monitor the synaptic junction between two neurons every 30 min. As shown in Fig. 9, distinct
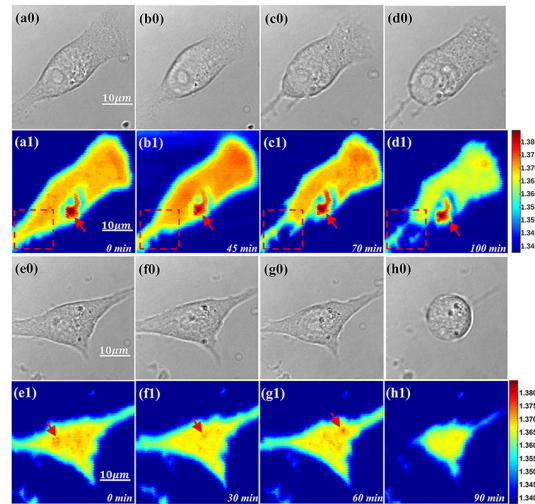
Fig. 8. Bright field images ($40\mu m \times 40\mu m$) of a U-87 cell at (a1) 0 min, (b0) 45 min, (c0) 75 min, and (d0) 100 min, and (a1-d1) corresponding RI images. (e0-h0) Bright-field images ($40\mu m \times 40\mu m$) of a U-87 cell treated with paclitaxel, and (e1-h1) corresponding RI images.

morphological changes were observed; in particular, a small part of the synapse marked with a square in Fig. 9(a1) was absent in Fig. 9(b1), which can be attributed to cellular communication. Moreover, the high-RI area marked with red circles highlights the decomposition of a subcellular structure and its movement toward the nucleolus. The dynamic process recorded using RIQM in Fig. 9(a1-b1) reveal the information transfer between two neurocytoma cells that cannot be easily identified from morphological changes in conventional bright-field images (Fig. 9(a0-b0)).

4. Conclusions

This study introduced a high-performance RIQM for label-free, non-invasive imaging of living cells, which simultaneously achieves high spatial resolution and RI sensitivity. The technique uses a POV beam with azimuthal polarization and first-order spiral phase to obtain the smallest focusing spot, and a lock-in amplifier to improve the signal-to-noise ratio. Cellular RI variation directly results from the density fluctuations of cellular dry mass, making RI a powerful endogenous contrast agent. Nevertheless, the applications of RIQM for cell studies including monitoring cell contraction, apoptosis and synapse growth were demonstrated which indicates RIQM is a promising quantitative phase imaging method with potential applications in biological sensing and imaging.
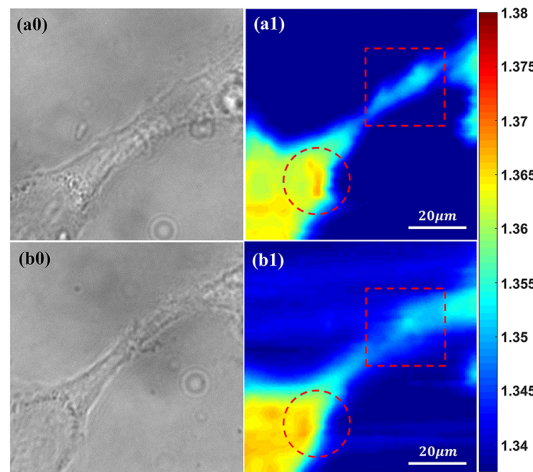
Fig. 9. (a0-b0) Bright-field images of a synapse between two U-87 MG cells, and (a1-b1) corresponding RI images after Gaussian smoothing ($40\mu m \times 40\mu m$). The region marked with a square contains a synapse and the region marked with a circle contains an organelle.

Disclosures

The authors declare no conflicts of interest.

See Supplement 1 for supporting content.

References

1. Z. U. Khan, E. Martín-Montanez, I. Navarro-Lobato, and E. C. Muly, "Memory deficits in aging and neurological diseases," Prog. Mol. Biol. Transl. Sci. **122**, 1–29 (2014).
2. T. A. Ulrich, E. M. De Juan Pardo, and S. Kumar, "The mechanical rigidity of the extracellular matrix regulates the structure, motility, and proliferation of glioma cells," Cancer Res. **69**(10), 4167–4174 (2009).
3. A. A. Khalili and M. R. Ahmad, "A Review of cell adhesion studies for biomedical and biological applications," Int. J. Mol. Sci. **16**(8), 18149–18184 (2015).
4. J. M. Muncie and V. M. Weaver, *The Physical and Biochemical Properties of the Extracellular Matrix Regulate Cell Fate*, 1st ed., vol. 130 (Elsevier Inc., 2018).
5. Z. Lansky, Y. Mutsafi, L. Houben, T. Ilani, G. Armony, S. G. Wolf, and D. Fass, "3D mapping of native extracellular matrix reveals cellular responses to the microenvironment," J. Struct. Biol. **1**, 100002 (2019).
6. Y. Kuai, J. Chen, X. Tang, Y. Xiang, F. Lu, C. Kuang, L. Xu, W. Shen, J. Cheng, H. Gui, G. Zou, P. Wang, H. Ming, J. Liu, X. Liu, J. R. Lakowicz, and D. Zhang, "Label-free surface-sensitive photonic microscopy with high spatial resolution using azimuthal rotation illumination," Sci. Adv. **5**(3), eaav5335–11 (2019).

7. S. W. Hell, S. J. Sahl, M. Bates, X. Zhuang, R. Heintzmann, M. J. Booth, J. Bewersdorf, G. Shtengel, H. Hess, P. Tinnefeld, A. Honigmann, S. Jakobs, I. Testa, L. Cognet, B. Lounis, H. Ewers, S. J. Davis, C. Eggeling, D. Klenerman, K. I. Willig, G. Vicidomini, M. Castello, A. Diaspro, and T. Cordes, "The 2015 super-resolution microscopy roadmap," J. Phys. D: Appl. Phys. **48**(44), 443001 (2015).
8. Z. Liu, J. Liu, X. Wang, F. Mi, D. Wang, and C. Wu, "Fluorescent bioconjugates for super-resolution optical nanoscopy," Bioconjugate Chem. **31**(8), 1857–1872 (2020).
9. D. Axelrod, "Cell-substrate contacts illuminated by total internal reflection fluorescence," J. Cell Biol. **89**(1), 141–145 (1981).
10. A. L. Mattheyses, S. M. Simon, and J. Z. Rappoport, "Imaging with total internal reflection fluorescence microscopy for the cell biologist," J. Cell Sci. **123**(21), 3621–3628 (2010).
11. M. Cardoso Dos Santos, R. Déturche, C. Vézy, and R. Jaffiol, "Topography of cells revealed by variable-angle total internal reflection fluorescence microscopy," Biophys. J. **111**(6), 1316–1327 (2016).
12. J. Liu, Q. Li, M. Li, S. Gao, C. Liu, L. Zou, and J. Tan, "Elliptical mirror-based TIRF microscopy with shadowless illumination and adjustable penetration depth," Opt. Lett. **42**(13), 2587 (2017).
13. C. Liu, M. Malek, I. Poon, L. Jiang, A. M. Siddiquee, C. J. R. Sheppard, A. Roberts, H. Quiney, D. Zhang, X. Yuan, J. Lin, C. Depeursinge, P. Marquet, and S. S. Kou, "Simultaneous dual-contrast three-dimensional imaging in live cells via optical diffraction tomography and fluorescence," Photonics Res. **7**(9), 1042 (2019).
14. T. A. Zangle and M. A. Teitell, "Live-cell mass profiling: An emerging approach in quantitative biophysics," Nat. Methods **11**(12), 1221–1228 (2014).
15. Y. K. Park, M. Diez-Silva, G. Popescu, G. Lykotrafitis, W. Choi, M. S. Feld, and S. Suresh, "Refractive index maps and membrane dynamics of human red blood cells parasitized by Plasmodium falciparum," Proc. Natl. Acad. Sci. U. S. A. **105**(37), 13730–13735 (2008).
16. Y. K. Park, C. Depeursinge, and G. Popescu, "Quantitative phase imaging in biomedicine," Nat. Photonics **12**(10), 578–589 (2018).
17. F. Zernike, "The concept of degree of coherence and its application to optical problems," Physica **5**(8), 785–795 (1938).
18. F. Zernike, "Observation of transparent objects," Physica **9**(10), 974–986 (1942).
19. R. D. Allen, G. B. David, and G. Nomarski, "The Zeiss-Nomarski differential interference equipment for transmitted-light microscopy," (1969).
20. J. E. Malamy and M. Shribak, "An orientation-independent DIC microscope allows high resolution imaging of epithelial cell migration and wound healing in a cnidarian model," J. Microsc. **270**(3), 290–301 (2018).
21. T. H. Nguyen, M. E. Kandel, M. Rubessa, M. B. Wheeler, and G. Popescu, "Gradient light interference microscopy for 3D imaging of unlabeled specimens," Nat. Commun. **8**(1), 210 (2017).
22. G. Popescu, L. P. Deflores, J. C. Vaughan, K. Badizadegan, H. Iwai, R. R. Dasari, and M. S. Feld, "Fourier phase microscopy for investigation of biological structures and dynamics," Opt. Lett. **29**(21), 2503 (2004).
23. T. Ikeda, G. Popescu, R. R. Dasari, and M. S. Feld, "Hilbert phase microscopy for investigating fast dynamics in transparent systems," Opt. Lett. **30**(10), 1165 (2005).
24. J. Reed, J. J. Troke, J. Schmit, S. Han, M. A. Teitell, and J. K. Gimzewski, "Live cell interferometry reveals cellular dynamism during force propagation," ACS Nano **2**(5), 841–846 (2008).
25. Z. Wang, H. Ding, and G. Popescu, "Spatial light interference microscopy (SLIM)," Opt. Express **19**(2), 1016 (2011).
26. S. Chowdhury, M. Chen, R. Eckert, D. Ren, F. Wu, N. Repina, and L. Waller, "High-resolution 3D refractive index microscopy of multiple-scattering samples from intensity images," Optica **6**(9), 1211 (2019).
27. J. Li, A. Matlock, Y. Li, Q. Chen, C. Zuo, and L. Tian, "High-speed in vitro intensity diffraction tomography," Adv. Photonics **1**(06), 1 (2019).
28. K. J. Moh, X.-C. Yuan, J. Bu, S. W. Zhu, and B. Z. Gao, "Surface plasmon resonance imaging of cell-substrate contacts with radially polarized beams," Opt. Express **16**(25), 20734 (2008).
29. S. Pechprasarn and M. G. Somekh, "Surface plasmon microscopy: Resolution, sensitivity and crosstalk," J. Microsc. **246**(3), 287–297 (2012).
30. A. W. Peterson, M. Halter, A. Tona, and A. L. Plant, "High resolution surface plasmon resonance imaging for single cells," BMC Cell Biol. **15**(1), 35 (2014).
31. A. R. Halpern, J. B. Wood, Y. Wang, and R. M. Corn, "Single-nanoparticle near-infrared surface plasmon resonance microscopy for real-time measurements of DNA hybridization adsorption," ACS Nano **8**(1), 1022–1030 (2014).
32. L. Berguiga, L. Streppa, E. Boyer-Provera, C. Martinez-Torres, L. Schaeffer, J. Elezgaray, A. Arneodo, and F. Argoul, "Time-lapse scanning surface plasmon microscopy of living adherent cells with a radially polarized beam," Appl. Opt. **55**(6), 1216 (2016).
33. E. Kreysing, H. Hassani, N. Hampe, and A. Offenhäusser, "Nanometer-resolved mapping of cell-substrate distances of contracting cardiomyocytes using surface plasmon resonance microscopy," ACS Nano **12**(9), 8934–8942 (2018).
34. K. Toma, H. Kano, and A. Offenhäusser, "Label-free measurement of cell-electrode cleft gap distance with high spatial resolution surface plasmon microscopy," ACS Nano **8**(12), 12612–12619 (2014).
35. F. Meng, L. Du, A. Yang, S. Wei, T. Lei, D. Zhang, and X. Yuan, "Metal-dielectric waveguide structure supporting an evanescent wave with long propagation distance in an aqueous environment," J. Phys. D: Appl. Phys. **50**(44), 445101 (2017).

36. L. Sun, Y. Zhang, Y. Wang, C. Zhang, C. Min, Y. Yang, S. Zhu, and X. Yuan, "Refractive index mapping of single cells with a graphene-based optical sensor," Sens. Actuators, B **242**, 41–46 (2017).

37. L. Sun, Y. Zhang, Y. Wang, Y. Yang, C. Zhang, X. Weng, S. Zhu, and X. Yuan, "Real-time subcellular imaging based on graphene biosensors," Nanoscale **10**(4), 1759–1765 (2018).

38. L. Sun, Y. Zhang, C. Zhang, Y. Dai, Z. Xin, S. Zhu, X. Yuan, C. Min, and Y. Yang, "Refractive index sensing and imaging based on polarization-sensitive graphene," Opt. Express **27**(20), 29273 (2019).

39. L. Sun, Y. Zhang, H. Chen, C. Zhang, Y. Fu, S. Zhu, Y. Yang, C. Min, and X. Yuan, "Generalized vector diffraction model for tight focusing of light with arbitrary polarization state," Optik **201**, 163528 (2020).

40. M. Born and E. Wolf, *Principles of Optics:Electromagnetic Theory of Propagation, Interference and Diffraction of Light*, 7th ed. (Cambridge University Press, 1999).

41. M. McClimans, C. LaPlante, D. Bonner, and S. Bali, "Real-time differential refractometry without interferometry at a sensitivity level of 10-6," Appl. Opt. **45**(25), 6477–6486 (2006).

42. K. P. Bohannon, R. W. Holz, and D. Axelrod, "Refractive Index imaging of cells with variable-angle near-total internal reflection (TIR) microscopy," Microsc. Microanal. **23**(5), 978–988 (2017).

43. A. Xia, S. Yang, R. Zhang, L. Ni, X. Xing, and F. Jin, "Imaging the Separation Distance between the Attached Bacterial Cells and the Surface with a Total Internal Reflection Dark-Field Microscope," Langmuir **35**(26), 8860–8866 (2019).

44. R. Parthasarathy and J. T. Groves, "Optical techniques for imaging membrane topography," Cell Biochem. Biophys. **41**(3), 391–414 (2004).

45. K. Lam Hui, C. Wang, B. Grooman, J. Wayt, and A. Upadhyaya, "Membrane dynamics correlate with formation of signaling clusters during cell spreading," Biophys. J. **102**(7), 1524–1533 (2012).

46. W. M. Ash and M. K. Kim, "Digital holography of total internal reflection," Coherent Opt. Technol. Appl. COTA **16**, 9CTuA4 (2008).

47. W. M. Ash, L. Krzewina, and M. K. Kim, "Quantitative imaging of cellular adhesion by total internal reflection holographic microscopy," Appl. Opt. **48**(34), H144 (2009).10.1364/AO.48.00H144

48. A. Calabuig, M. Matrecano, M. Paturzo, and P. Ferraro, "Common-path configuration in total internal reflection digital holography microscopy," Opt. Lett. **39**(8), 2471 (2014).

49. B. Mandracchia, O. Gennari, V. Marchesano, M. Paturzo, and P. Ferraro, "Label free imaging of cell-substrate contacts by holographic total internal reflection microscopy," J. Biophotonics **10**(9), 1163–1170 (2017).

50. B. Mandracchia, O. Gennari, A. Bramanti, S. Grilli, and P. Ferraro, "Label-free quantification of the effects of lithium niobate polarization on cell adhesion via holographic microscopy," J. Biophotonics **11**(8), e201700332–6 (2018).

51. A. S. Ostrovsky, C. Rickenstorff-Parrao, and V. Arrizón, "Generation of the "perfect" optical vortex using a liquid-crystal spatial light modulator," Opt. Lett. **38**(4), 534 (2013).

52. J. García-García, C. Rickenstorff-Parrao, and A. S. Ostrovsky, "Simple technique for the perfect vortex generation," Lat. Am. Opt. Photonics Conf. LAOP **39**, LTu4A.10 (2014).

53. P. Vaity and L. Rusch, "Perfect vortex beam: Fourier transformation of a Bessel beam," Opt. Lett. **40**(4), 597 (2015).

54. C. Zhang, C. Min, L. Du, and X. C. Yuan, "Perfect optical vortex enhanced surface plasmon excitation for plasmonic structured illumination microscopy imaging," Appl. Phys. Lett. **108**(20), 201601 (2016).

55. Z. Xin, C. Zhang, and X. Yuan, "Concentric perfect optical vortex beam generated by a digital micromirrors device," IEEE Photonics J. **9**(2), 1–7 (2017).

56. E. Wolf, "Electromagnetic diffraction in optical systems, II. Structure of the image field in an aplanatic system," Proc. R. Soc. Lond. A **253**(1274), 358–379 (1959).

57. K. S. Youngworth and T. G. Brown, "Focusing of high numerical aperture cylindrical-vector beams," Opt. Express **7**(2), 77 (2000).

58. M. Leutenegger, R. Rao, R. A. Leitgeb, and T. Lasser, "Fast focus field calculations," Opt. Express **14**(23), 11277 (2006).

59. R. H. Renard, "Total Reflection: A New Evaluation of the Goos-Hänchen Shift," J. Opt. Soc. Am. **54**(10), 1190 (1964).

60. K. Y. Bliokh and A. Aiello, "Goos-Hänchen and Imbert-Fedorov beam shifts: An overview," J. Opt. **15**(1), 014001 (2013).

61. T. Demuth and M. E. Berens, "Molecular mechanisms of glioma cell migration and invasion," J. Neuro-Oncol. **70**(2), 217–228 (2004).

62. W. Xu, R. Mezencev, B. Kim, L. Wang, J. McDonald, and T. Sulchek, "Cell Stiffness Is a Biomarker of the Metastatic Potential of Ovarian Cancer Cells," PLoS One **7**(10), e46609 (2012).

63. S. V. Bava, C. N. Sreekanth, A. K. T. Thulasidasan, N. P. Anto, V. T. Cheriyan, V. T. Puliyappadamba, S. G. Menon, S. D. Ravichandran, and R. J. Anto, "Akt is upstream and MAPKs are downstream of NF-κB in paclitaxel-induced survival signaling events, which are down-regulated by curcumin contributing to their synergism," Int. J. Biochem. Cell Biol. **43**(3), 331–341 (2011).

64. P. B. Schiff and S. B. Horwitz, "Taxol stabilizes microtubules in mouse fibroblast cells," Proc. Natl. Acad. Sci. U. S. A. **77**(3), 1561–1565 (1980).

65. Z. G. Luo, "Synapse formation and remodeling," Sci. China: Life Sci. **53**(3), 315–321 (2010).